

# A Multilevel Guidance-Exploration Network and Behavior-Scene Matching Method for Human Behavior Anomaly Detection

Guoqing Yang<sup>1</sup> Zhiming Luo<sup>1</sup> Jianzhe Gao<sup>1</sup> Yingxin Lai<sup>1</sup>  
 Kun Yang<sup>1</sup> Yifan He<sup>2</sup> Shaozi Li<sup>1</sup>  
<sup>1</sup> Xiamen University, Xiamen, China; <sup>2</sup> Reconova Technologies, China

## Abstract

Human behavior anomaly detection aims to identify unusual human actions, playing a crucial role in intelligent surveillance and other areas. The current mainstream methods still adopt reconstruction or future frame prediction techniques. However, reconstructing or predicting low-level pixel features easily enables the network to achieve overly strong generalization ability, allowing anomalies to be reconstructed or predicted as effectively as normal data. Different from their methods, inspired by the Student-Teacher Network, we propose a novel framework called the Multilevel Guidance-Exploration Network (MGENet), which detects anomalies through the difference in high-level representation between the Guidance and Exploration network. Specifically, we first utilize the pre-trained Normalizing Flow that takes skeletal keypoints as input to guide an RGB encoder, which takes unmasked RGB frames as input, to explore motion latent features. Then, the RGB encoder guides the mask encoder, which takes masked RGB frames as input, to explore the latent appearance feature. Additionally, we design a Behavior-Scene Matching Module (BSMM) to detect scene-related behavioral anomalies. Extensive experiments demonstrate that our proposed method achieves state-of-the-art performance on ShanghaiTech and UBnormal datasets, with AUC of 86.9 % and 73.5 %, respectively. The code will be available on <https://github.com/moluggg/GENet>.<sup>1</sup>

## 1. Introduction

Human behavior anomaly detection aims to temporally or spatially localize the abnormal actions of the person within a video. It plays a significant role in enhancing public security [30, 37]. Detecting such anomalies presents a challenge due to the infrequent occurrence and the various types of abnormal events [43]. As a result, most typical methods [6, 16, 20, 25, 33, 42], employ unsupervised learning

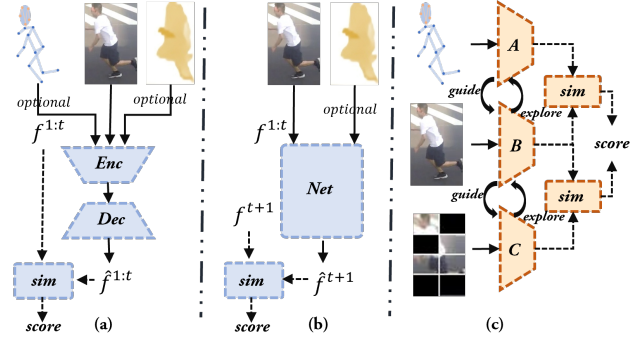


Figure 1. Comparison of different methods using various features. (a) Reconstruction-based method, using the autoencoder to reconstruct the previous  $T$  frames  $f^{1:t}$ . (b) Prediction-based method, predicting the  $t + 1$  frame  $f^{t+1}$  from the prior  $T$  frames. Both of them detect anomalies based on reconstruction or prediction errors. (c) Our Multilevel Guidance-Exploration framework, includes two similar levels. For instance, in the 1-st level, Encoder-B learns another type of feature under the guidance of a pre-trained network (Encoder-A), detecting anomalies based on the similarity of latent output features.

approaches using only normal data for training. In these approaches, including our method, behaviors that the model identifies as outliers are considered anomalies.

Many unsupervised methods often use reconstruction or future frame prediction methods combined with various features to detect human behavior anomalies. The reconstruction-based framework [14, 21, 25, 26, 35], illustrated in Figure 1(a), utilizes autoencoders trained on normal data, detecting anomalies based on elevated reconstruction errors. [35] propose a new autoencoder model, named Spatio-Temporal Auto-Trans-Encoder, to enhance consecutive frame reconstruction. As depicted in Figure 1(b), the prediction-based methods [4, 6, 17, 20, 21, 42] typically predict pixel-level features for the next frame using previous frames. [6] propose an Appearance-Motion Memory Consistency Network based on autoencoders, explicitly considering the endogenous consistency semantics between

<sup>1</sup>ygq.qingdao@163.com

optical flow features and RGB appearance features during the prediction process. Additionally, Liu et al. [21] use a hybrid strategy by initially reconstructing optical flow features with a reconstruction autoencoder and then jointly predicting the next frame with previous frames.

However, reconstructing or predicting pixel-level features at a low level can result in the network having overly strong generalization [6, 25, 33, 42], where some anomalous samples can be reconstructed or predicted as effectively as normal samples. This phenomenon poses a challenge in distinguishing between normal and anomalous instances. Additionally, these approaches [4, 14–17, 21, 33] ignore scene context. They focus solely on the behavior of individuals without considering their interaction with the surrounding scene. For example, lying on a zebra-crossing road is more likely to be considered anomalous compared to the same posture on a beach setting.

Different from existing methodologies, we propose an innovative unsupervised behavior anomaly detection framework named Multilevel Guided Exploration Network(MGENet), which focuses on exploring high-level feature difference rather than recovering or predicting pixel-level information. As shown in Figure. 1(c), MGENet detects motion and appearance anomalies using a Two-level guidance-exploration pattern. Each level is trained with different types of input features and leverages the difference in output features between the Guidance and Exploration Networks to detect anomalies. This design makes it challenging for anomalies to exhibit performance similar to normal samples.

Specifically, we employ Spatio-temporal Normalizing Flow [16] to map normal human-pose data into a latent representation characterized by a Gaussian distribution. This process strategically situates anomalous pose data at the distribution’s periphery. Then, guided by Normalizing Flow, the RGB Encoder captures spatio-temporal features, detecting motion anomalies by analyzing the difference in the output features between these two networks. Furthermore, the RGB Encoder also guides the unmask Encoder to distill high-level features from specific patches of masked RGB frames, detecting appearance anomalies based on the similarity between the high-level features output by both networks. Additionally, we incorporate a Behavior-Scene matching module, which establishes and stores the relationship between normal behavior and scenes, enabling the detection of scene anomalies. We demonstrate the effectiveness of the method on two publicly available datasets.

In summary, the contributions of our work are as follows:

- Different from reconstruction or prediction methods, we design a novel framework to detect not only motion and appearance anomalies but also scene-related anomalies.
- We design a novel multilevel guidance-exploration pattern for detecting anomalies based on the high-level fea-

ture differences between two levels of guidance and exploration networks.

- We propose a behavior-scene matching method to store the relationship between scenes and behaviors and can detect scene-related anomalies.
- Extensive experiments demonstrate that our proposed method outperforms existing unsupervised methods, achieving a state-of-the-art AUC of 86.9% on the ShanghaiTech dataset and 73.5% on the UBnormal dataset.

## 2. Related Work

### 2.1. Video Anomaly Detection

In recent years, numerous studies have achieved remarkable results based on RGB frames, optical flow, or pose features.

Some researchers employ reconstruction methods[14, 21, 25, 26, 30], for anomaly detection, assessing anomalies based on higher reconstruction errors compared to normal samples. Park et al. [25] propose augmenting the autoencoder with a memory module, favoring proximity to normal samples during reconstruction and amplifying errors for anomalies. Sun and Gong [30] utilize two autoencoders to reconstruct motion and appearance features. Furthermore, they also design a contrastive learning method to identify scene-related behavioral anomalies, but they only detect within limited scenarios, lacking diversity. Some researchers use prediction methods[4, 6, 17, 20, 21, 42], to detect anomalies. Liu et al. [20] propose a future frame prediction approach, which detects anomalies by assessing the discrepancies between predicted images and actual images. Chen et al. [8] find limitations in simple prediction constraints for representing appearance and flow features. They introduce a novel bidirectional architecture with three consistency constraints to regulate the prediction task. Yang et al. [42] introduced the task of key frame restoration, encouraging Deep Neural Networks to infer missing frames based on video key frames, thereby restoring the video.

Furthermore, in recent years, there has been an emergence of utilizing alternative methods for anomaly detection. Hirschorn et al. [16] employ Normalizing Flow to map normal data into the latent representation, locating anomalous data at the distribution periphery. Wang et al. [33] propose a new pretext task, disrupting both temporal and spatial order and training the model to restore RGB frames.

### 2.2. Student Teacher Network

Recently, in the field of industrial anomaly detection, some researchers [27] employ knowledge distillation to detect anomalies by utilizing the regression error of student networks on the feature outputs of a high-parameter teacher network. Specifically, the STPM method [40] is based on student-teacher feature pyramid matching, with the student and teacher networks being pre-trained as ResNet50 and

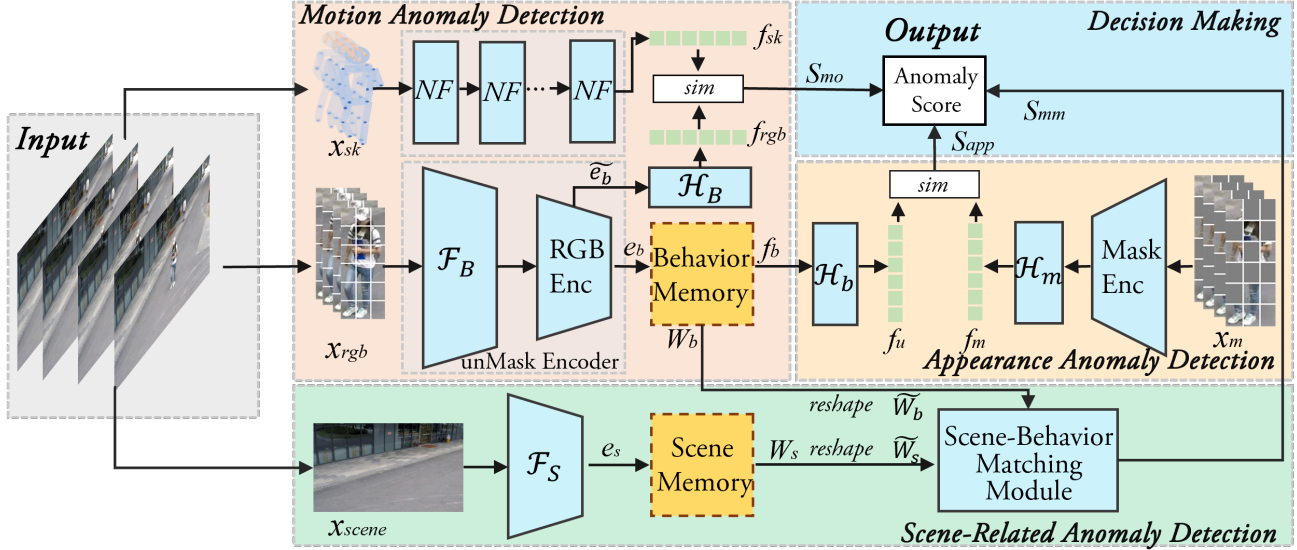


Figure 2. The overall framework of our method.

ResNet18, respectively. In this scenario, the student model, with fewer parameters, closely approximates the teacher’s performance on normal data but exhibits notable disparities when encountering unseen anomalous data.

The methods mentioned earlier and our approach’s appearance anomaly detection phase share similarities, employing knowledge distillation. However, there’s a difference in the motion anomaly detection process, where knowledge distillation is not the primary emphasis. The Normalizing Flow has a lightweight architecture, whereas the RGB Encoder has a more complex structure. Additionally, there are substantial differences in the frameworks and input data types between these two networks.

### 2.3. Masked Visual Model

Masked Visual Modeling [36] improves visual representation learning by masking image portions. Chen et al. [9] propose a pretraining method with two tasks: predicting representations for masked patches and reconstructing masked patches. Zhang et al. [44] demonstrate improved performance with only supervised visible patches, omitting the need for masked patches. In the realm of video representation learning, Tong et al. [32] show that video-masked autoencoders are also data-efficient learners for self-supervised video pre-training. Wang et al. [34] present Masked Video Distillation, a succinct two-stage framework, for video representation learning. Inspired by masking tasks, we mask partially video frames and exclusively use visible frames to learn the latent high-level features of the uncovered frames. In this way, since the model has not encountered the appearance of anomalies before, there will be differences in the latent representation of unmasked frames.

## 3. Method

### 3.1. Overview

Figure 2 illustrates the overall framework. Given a video clip with  $T$  consecutive frames, we extract human-centric RGB frames  $x_{rgb} \in \mathbb{R}^{T \times H \times W \times C}$  and  $V$ -joints skeletal pose data  $x_{sk} \in \mathbb{R}^{T \times V \times C}$  [11, 39]. Meanwhile, according to BEIT [3], we segment the RGB frames into  $P$  patches and mask the rate of  $\gamma$  of the patches to obtain  $x_m$ . Then, anomalies are detected through the following four processes.

**Motion Anomaly Detection:** First, we pre-train Normalizing Flow to project  $x_{sk}$  into a latent representation  $f_{sk} \in \mathbb{R}^{T \times C_{mo}}$  following the Gaussian distribution. Then, it guides the RGB Encoder and head  $\mathcal{H}_B$  using RGB frames to learn spatio-temporal features  $f_{rgb} \in \mathbb{R}^{T \times C_{mo}}$

**Appearance Anomaly Detection:** Behavior Features  $e_b$  pass through behavior memory to obtain feature  $f_b$ , then we use head  $\mathcal{H}_u$  to map  $f_b$  into  $f_u \in \mathbb{R}^{T \times C_{app}}$ . Following this, it guides the Mask Encoder using masked RGB frames  $x_m$  to learn appearance features  $f_m \in \mathbb{R}^{T \times C_{app}}$ .

**Scene-related Anomaly Detection:** The scene undergoes feature extraction  $\mathcal{F}_S$  to generate scene features, alongside corresponding behavior features, pass through the memory banks to get soft addressing weights  $W_b \in \mathbb{R}^{P \times N_b}$  and  $W_s \in \mathbb{R}^{1 \times N_s}$ , respectively. Here,  $N_b$  and  $N_s$  represent the number of slots in the Behavior and Scene Memory, respectively. Then, they pass into the Behavior-Scene Matching Module together to compute the scene-related anomaly score  $S_{mm}$ .

**Anomaly Score:** The score is computed by considering

the difference between the pose feature  $f_{sk}$  and the behavior feature  $f_{rgb}$ , the similarity of appearance features  $f_u$  and  $f_m$ , and the matching score  $S_{mm}$ .

### 3.2. Motion Anomaly Detection

Skeletal data helps the model capture the essential characteristics of movements or postures [18, 41]. Recently, Hirschorn et al. [16] designed the Spatio-temporal Normalizing Flow ( $NF_s$ ), including  $L$  flow modules, which can map the skeletal distribution of normal skeletal data to a standard distribution through a series of invertible transformations, with anomalies typically found at the distribution’s periphery.

Building on the above rationale, firstly, we train Spatio-temporal Normalizing Flow according to [16], mapping pose data  $x_{sk}$  to latent behavior features  $f_{sk}$ :

$$f_{sk} = NF_s(x_{sk}). \quad (1)$$

Secondly, we use it as a pre-trained model to guide the exploration network (RGB Encoder) to generate the latent motion features  $f_{rgb}$ . The following are the detailed steps:

First, given RGB frames  $x_{rgb} \in \mathbb{R}^{T \times H \times W \times C}$ , similar to cube embedding [2, 10, 32], we treat each cube of  $2 \times 8 \times 8$  as one token embedding, and obtain  $t \times h \times w$  3D tokens, where  $t = \frac{T}{2}, h = \frac{H}{8}, w = \frac{W}{8}$ . Then, map each token to the channel dimension. Next, we pre-extract RGB features of these tokens and employ the RGB Encoder, a ViT backbone with joint space-time attention [10, 32], to obtain spatio-temporal features  $e_b \in \mathbb{R}^{P \times C_b}$ , where  $P = t \cdot h \cdot w$ .

Then, we reshape  $e_b$  into  $\tilde{e}_b \in \mathbb{R}^{t \times C_b \times h \times w}$  and design the spatial-temporal head  $\mathcal{H}_B$ , which replaces the  $3 \times 3 \times 3$  convolution in Spatial-Temporal Excitation [7] with the decomposed Large kernel Attention, named large Spatial-Temporal Attention (LSTA), to further capture the spatio-temporal relationships of patches with long-distance temporal dependencies and spatial variations in different frames of human actions.

In detail, spatio-temporal head  $\mathcal{H}_B$  consists of  $L$  LSTA modules and the MLP layers. As shown in Figure 3, given an input tensor  $e_b^{in} \in \mathbb{R}^{t \times c \times h \times w}$ , we begin by performing channel-wise averaging, yielding a global spatio-temporal tensor  $f \in \mathbb{R}^{t \times 1 \times h \times w}$ . Then, we reshape  $f$  into  $f^* \in \mathbb{R}^{1 \times t \times h \times w}$  and pass it through the 3DLKA module to get transformed tensor  $f_o^* \in \mathbb{R}^{1 \times t \times h \times w}$ , which is represented as follows:

$$f_o^* = 3DLKA(f^*) = CONV(DWDC(DWC(f^*))), \quad (2)$$

where  $DWC$  denotes a  $\frac{k}{d} \times \frac{k}{d} \times \frac{k}{d}$  deep dilated convolution with dilated  $d$ ,  $DWDC$  denotes a  $(2d-1) \times (2d-1) \times (2d-1)$  deep convolution, and  $CONV$  denotes a  $1 \times 1 \times 1$  convolution. Subsequently,  $f_o^*$  is reshaped to  $f_o \in \mathbb{R}^{t \times 1 \times h \times w}$  and

passed through a sigmoid activation function to obtain the attention map. Finally, we use this map to guide  $e_b^o$  for obtaining behavior feature  $e_b^o$ :

$$e_b^o = e_b^{in} + e_b^{in} \odot \text{sigmoid}(f_o), \quad (3)$$

where  $\odot$  denotes the element-wise product. After passing through the MLP layers, we obtain the motion feature  $f_{rgb}$ . Finally, we minimize the difference between  $f_{sk}$  and  $f_{rgb}$  feature to facilitate the model in learning spatio-temporal pose features of normal patterns.

$$\mathcal{L}_{mo} = \|f_{sk} - f_{rgb}\|_2^2. \quad (4)$$

In this way, for anomalous samples, achieving similar high-level semantic representation is more challenging due to differences in feature modalities and network architectures. Therefore, we can detect action anomalies based on the difference between the two types of features.

### 3.3. Appearance Anomaly Detection

Beyond motion anomalies, our method considers appearance anomalies, including carrying unidentified objects or using inappropriate vehicles. We extend Masked Image Modeling (MIM) [38] to video anomaly detection, enabling the Mask Encoder to learn normal appearance features guided by the unmasked RGB Encoder. This adaptation tackles challenges faced by the Mask Encoder in capturing high-level features of patches that were not encountered before but now are masked, resulting in noticeable differences from unmasked RGB features.

Specifically, following the approach of BEIT MASK [3], we mask patches with a ratio  $\gamma$ , which is set to 50% and obtain masked RGB frames  $x_m$ . Noted that we used the same mask for the frames within the same video frame, preventing the model from extracting patch features from adjacent frames.

$$\{x_m^1, x_m^2, \dots, x_m^{P/2}\} = \text{MASK}\{x_{rgb}^1, x_{rgb}^2, \dots, x_{rgb}^P\}, \quad (5)$$

where  $P$  denotes the number of patches. Next, we also use the cube embedding method described in Section 3.2 to obtain tokens. These tokens pass through the Mask Encoder, which has a structure similar to the RGB Encoder, to learn appearance features. Then, the projection head is employed to obtain latent appearance features, denoted as  $f_m$ . Simultaneously, the appearance features  $f_b$  also undergo the projection head to obtain latent appearance features  $f_u$  with the same size as  $f_b$ .

During the training process, the RGB Encoder keeps fixed, while the Mask Encoder distills the high-level feature representation of the RGB Encoder under the condition of having only partially visible patches. The final loss function can be expressed as:

$$\mathcal{L}_{app} = 1 - \frac{f_m \cdot f_u}{\|f_m\| \cdot \|f_u\|}. \quad (6)$$



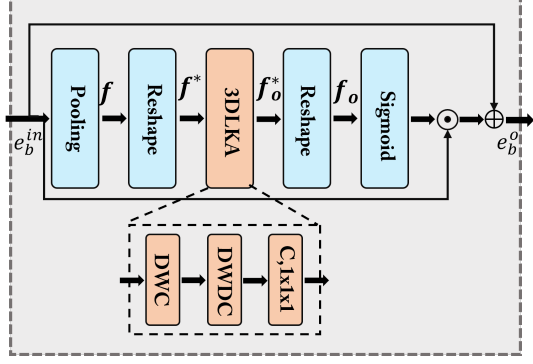


Figure 3. The framework of LSTA.

### 3.4. Scene-Related Anomaly Detection

Formally, we postulate that unobserved behaviors within a scene should be categorized as anomalies. To detect these anomalies, we design the Scene-Behavior Matching Module to capture the relationships between normal patterns of scenes and behaviors. As a result, scene-related behavior anomalies exhibit weaker matching with the learned features, leading to higher anomaly scores.

As illustrated in Figure. 4(a), the Behavior-Scene Matching Memory(BSMM), similar to the Behavior Memory and Scene Memory, is a read-write memory with a similar structure [25]. However, the key difference is that the Behavior-Scene Matching Memory stores the representation of the addressing weights in the Behavior Memory and Scene Memory for the behavioral features and their corresponding scene features of all normal data. Below is an introduction to its update and read processes.

First, the scene image passes through the feature extractor, generating scene features  $e^s \in \mathbb{R}^{C_s}$ . Then, behavior features  $e^b \in \mathbb{R}^{P \times C_b}$  and  $e^s$  query the Behavior Memory and Scene Memory, respectively, and then contribute to calculating the similarity weights  $W_b \in \mathbb{R}^{P \times N_b}$  and  $W_s \in \mathbb{R}^{1 \times N_s}$ , where  $N_b$  and  $N_s$  denote as the number of the slots in behavior memory and scene memory, respectively. For the  $i$ -th slot in behavior memory, denoted as  $\mathbf{m}_i^b \in \mathbf{M}^b$ , we can calculate the addressing weights between it and the  $p$ -th query  $e_p^b$  item as follows:

$$w_{i,p}^b = \frac{\exp(d(e_p^b, \mathbf{m}_i^b))}{\sum_{j=1}^{N_b} \exp(d(e_p^b, \mathbf{m}_j^b))}, \quad (7)$$

where  $d(e^*, m^*)$  denotes cosine similarity. The computation method for  $w_i^s \in W^s$  is the same as that for  $w_{i,p}^b$ .

**Update:** We reshape  $W^b$  and  $W^s$  into one-dimensional vectors  $\tilde{W}^b \in \mathbb{R}^{L_b}$  and  $\tilde{W}^s \in \mathbb{R}^{L_s}$ , where  $L_b = P \times C_b$  and  $L_s = 1 \times C_s$ . Then, concatenate  $\tilde{W}^b$  and  $\tilde{W}^s$  along the channel:

$$\mathbf{W}^r = [\tilde{W}^b, \tilde{W}^s]. \quad (8)$$

Next, similar to [25, 30], for each items  $\mathbf{m}_i^r \in \mathbf{M}^r$  in the Behavior-Scene Memory, we update as following:

$$\mathbf{m}_i^r \leftarrow f \left( \mathbf{m}_i^r + \sum_{v \in U^i} v^{p,i} \mathbf{W}_v^r \right), \quad (9)$$

where  $f(\cdot)$  is the  $L_2$  norm.  $U^i$  represents the set of indices for the corresponding queries for the  $i$ -th item in the memory.  $v^{p,i}$  represents matching probability between memory items and queries, similar to equation (7). It is worth noting that the aforementioned update operation occurs only in the final round and keeps the parameters of the Behavior Memory and Scene Memory unchanged.

**Read:** Different from the previous method[25], we compute the matching weights  $c_i^b \in C^b$  between  $W_b$  and the first  $N_b$  channels of the Matching Memory  $\mathbf{M}^r$ :

$$c_i^b = \frac{\exp(d(W^b, \mathbf{m}_{i,:L_b}^r))}{\sum_{j=1}^N \exp(d(W^b, \mathbf{m}_{j,:L_b}^r))}. \quad (10)$$

Similarly, we can use the above method with the last  $N_s$  channels of  $\mathbf{M}^r$  to calculate  $C^s$ .

In this way,  $W^b$  and  $W^s$  serve as vector representations of historical behaviors and scenes. Their combination stored in  $\mathbf{M}^r$  forms a pattern of the behavior-scene pattern. During the test phase,  $W^b$  and  $W^s$  act as query terms, individually computed with the behavioral and scene representations of each item  $\mathbf{m}_i^r$  in  $\mathbf{M}^r$  to derive  $c_i^b$  and  $c_i^s$ . If the difference between them is significant, it indicates a mismatch between the behavior and the current scene. Finally, anomalies are measured by considering all patterns stored in the Matching Memory.

### 3.5. Loss Function and Anomaly Score

**Loss Function:** The training loss includes the regression loss  $\mathcal{L}_{mo}$ , and the distillation loss  $\mathcal{L}_{app}$ . Additionally, to allocate similar queries to the same item, the objective is to reduce the number of items and the overall memory size according to [25], there is the feature separateness Loss defined with a margin of  $\epsilon$  as follows:

$$\mathcal{L}_{sep} = \sum_p^P \left[ \|\mathbf{W}_p^r - \mathbf{m}^{st}\|_2 - \|\mathbf{W}_p^r - \mathbf{m}^{nd}\|_2 + \epsilon \right]_+, \quad (11)$$

where  $P$  represents the number of queries, and  $\mathbf{m}^{st}$  and  $\mathbf{m}^{nd}$  represent the first and second nearest items for the query  $\mathbf{W}_p^r$ . Thus, for the three memories, the separateness loss is denoted as  $\mathcal{L}_{sep}^b$ ,  $\mathcal{L}_{sep}^s$ , and  $\mathcal{L}_{sep}^r$  respectively. In summary, the overall loss function is expressed as:

$$\mathcal{L} = \mathcal{L}_{mo} + \alpha \mathcal{L}_{app} + \beta (\mathcal{L}_{sep}^b + \mathcal{L}_{sep}^s + \mathcal{L}_{sep}^r), \quad (12)$$

where  $\alpha$  and  $\beta$  are balancing hyper-parameters.

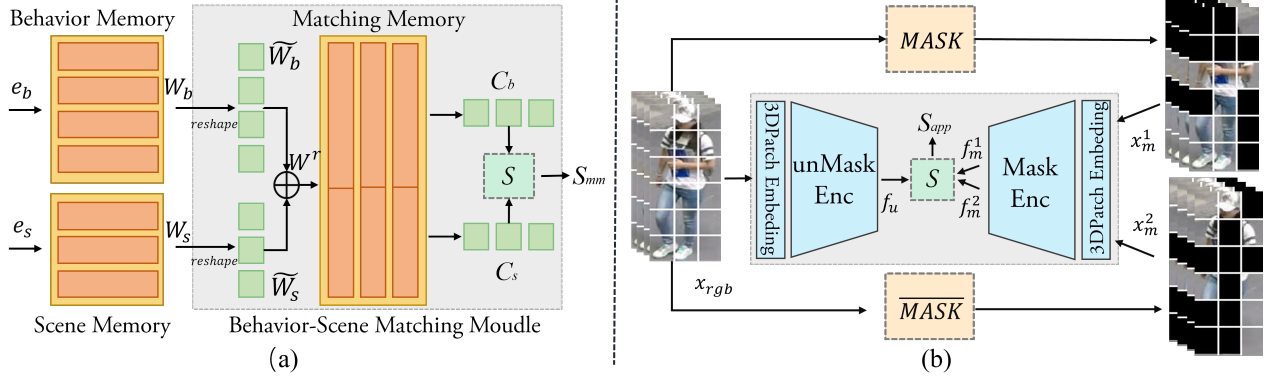


Figure 4. Calculation process of (a) scene-related anomaly score and (b) appearance anomaly score. Here,  $S$  represents similarity calculation,  $MASK$  and  $\overline{MASK}$  represent mutually opposite masks. Note that in figure(b), the two sets of masked images are sequentially processed through the Mask Encoder

**Anomaly Score:** Measuring the anomaly scores involves three components: motion anomaly score, appearance anomaly score, and scene-related anomaly score. In the first level of our framework, we obtain high-level skeleton feature  $f_{sk}$  and behavior feature  $f_{rgb}$ . Due to the distinct structures and input data of the two modules, When encountering previously unseen anomalous behaviors, there is a substantial difference between them, We can utilize this difference as the Motion Anomaly Score:

$$S_{mo} = \|f_{sk} - f_{rgb}\|. \quad (13)$$

Furthermore, as shown in Figure. 4(b), given the adoption of a 50% masking approach, there are two sets of mutually exclusive masks  $MASK$  and  $\overline{MASK}$  to ensure complete coverage for all patches. Therefore, the calculation method for appearance anomaly scores  $S_{app}$  is:

$$S_{app} = \frac{1}{2} sim(f_u, f_m^1) + \frac{1}{2} sim(f_u, f_m^2), \quad (14)$$

where  $sim(f_u, f_*) = 1 - f_u \cdot f_* / (\|f_u\| \cdot \|f_*\|)$ . Next, we can determine scene-related anomalies based on the difference in matching weights  $C_b$  and  $C_s$  between behavior and scene:

$$S_{mm} = \|C_b - C_s\|. \quad (15)$$

Taking all the above into consideration, the anomaly score for behavior can be expressed as:

$$Score = S_{mo} + \lambda_{app} S_{app} + \lambda_{mm} S_{mm}, \quad (16)$$

where  $\lambda_{app}$  and  $\lambda_{mm}$  are balancing hyperparameters. Finally, the scores are normalized to the range of 0-1 using min-max scaling. We employ the overlap sampling method, where the score of each video clip in a segment is used as the frame-level score for the intermediate frames.

## 4. Experiments

### 4.1. Datasets

In this study, we evaluate the performance of our proposed method on two public datasets. The **ShanghaiTech** [22] dataset is one of the largest datasets for video anomaly detection. The total number of frames used for training and testing is 274K and 42K, respectively. This dataset contains various abnormal types, such as fighting, running in inappropriate scenes, and others. The **UBnormal** [1] is a newly introduced supervised multi-scene large-scale video anomaly detection dataset. This dataset has diverse scenes, diverse clothing, and complex environments. Especially, the environments contain some changeling scenes, such as foggy days and fires. Following the approach of [16, 29], we remove anomalous video segments from the training set, retaining only normal video segments for model training.

### 4.2. Implementation Details & Evaluation Metric

All experiments are conducted using PyTorch on an NVIDIA RTX 3090. The Normalizing Flow is pre-trained using a flow number of  $L = 8$ . For the training of RGB Encoder and Mask Encoder, the SGD optimizer with a learning rate of 0.0001 and a momentum of 0.5 is utilized. Behavior, Scene, and Behavior-Scene Matching Memory each have 128, 32, and 64 memory items, respectively. The pre-trained model  $\mathcal{F}_B$  utilized the representation layers from the first two stages of the Video Swin Transformer model trained on the Kinetics-400 dataset. In the final loss function  $\mathcal{L}$ , the parameter  $\alpha$  is set to 0.1 and  $\beta$  to 0.001. In anomaly score  $Score$ , both  $\lambda_{app}$  and  $\lambda_{mm}$  are set to 0.1. The parametric experiments can be found in the Appendix.

We evaluate our method using the area under the ROC curve (AUC) at the frame level as the evaluation metric. The AUC score is calculated by connecting all frames and com-

Table 1. Comparison of AUC(%) Performance on ShanghaiTech(SHT) and UBnormal(UBN) datasets. We additionally list the input features of the approach, where  $f_{rgb}$  denotes appearance,  $f_o$  denotes optical flow and  $f_{sk}$  denotes pose data. **R**, **P**, **O** represent reconstruction, prediction, and other methods, respectively. (\*) indicates reproduction results. The best result (**bold**), and the second-best result (underlined).

	Algorithm	Type	Feature	SHT	UBN
<b>WE</b>	MIL [28]	-	$f_{rgb}$	85.3	62.1
	MIST [12]	-	$f_{rgb}$	94.8	68.2
	RTFM [31]	-	$f_{rgb}$	97.2	69.4
	MSL [19]	-	$f_{rgb}$	95.5	-
	LSTC [29]	-	$f_{rgb}$	97.8	77.5
	<b>UN</b>	MPEDRNN [24]	R	$f_{rgb}$	77.1
GPEC [23]		R	$f_{rgb}$	76.1	53.4
TimeSformer [5]		R	$f_{rgb}$	-	<u>69.8*</u>
DPU [35]		R	$f_o$	77.8	-
AED [15]		R	$f_{rgb}$	82.7	59.3
SSPCAB [26]		R	$f_{rgb}$	83.6	-
COSKAD [13]		R	$f_{sk}$	75.6	65.5
HSC [30]		R	$f_{rgb} + f_{sk}$	83.4	-
USTNDSC [42]		P	$f_{rgb}$	73.8	-
AMFT [6]		P	$f_{rgb} + f_o$	73.7	-
AMSRC [17]		P	$f_{rgb} + f_o$	76.6	-
SSMTL++ [4]		P+R	$f_{rgb} + f_o$	83.8	62.1
HF <sup>2</sup> -VAD [21]		P+R	$f_{rgb} + f_o$	76.2	65.2
STG-NF [16]		O	$f_{sk}$	<u>85.9</u>	69.7*
JIGSAW [33]		O	$f_{rgb}$	84.3	56.4*
<b>Ours</b>	O	$f_{rgb} + f_{sk}$	<b>86.9</b>	<b>73.5</b>	

puting the micro-averaged AUC score [16].

### 4.3. Comparison with Other Methods

Table 1 presents a comparison of our method with cutting-edge video anomaly detection methods published in recent years, including both some weakly supervised(WE) and unsupervised(UN) learning-based approaches. By analyzing the table, it can be observed that our method achieves impressive AUC scores of 86.9% on the ShanghaiTech dataset(SHT) and 73.5% on the UBnormal dataset(UBN). These scores surpass the previous state-of-the-art unsupervised learning method by 1.16% and 5.30%, respectively. Notably, our method also outperforms most of the weakly supervised learning methods on the UBnormal dataset. These results confirm the effectiveness of our proposed Multilevel Guidance-Exploration framework for human behavior anomaly detection tasks.

### 4.4. Visualization Evaluation

The anomaly scores in two distinct scenes from the ShanghaiTech and UBnormal datasets are visualized in Figure 5. The figure displays the results of our final method. The red area represents the time interval in which the ground-truth

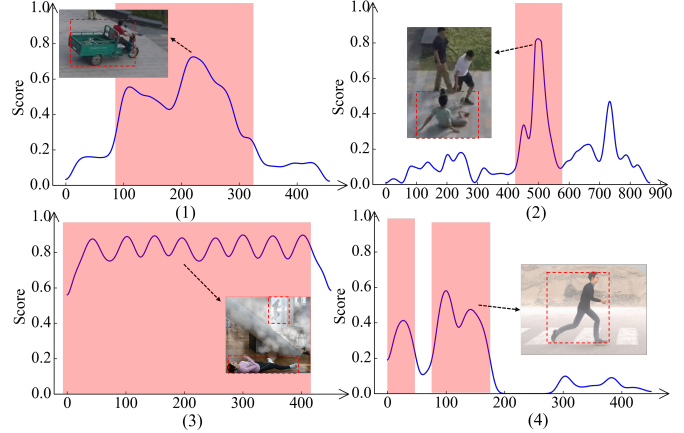


Figure 5. Visualizing Anomaly Scores for Video Frames 01–0053, 04–0004 from the ShanghaiTech Dataset, and *abnormal-scene-5-2-smoke*, *abnormal-scene-11-2-fog* from the UBnormal Dataset.

anomaly occurs.

**Appearance Anomaly:** Figure 5 (1) depicts an anomaly where a person is riding an electric scooter on a pedestrian path. Although "sitting" appears to be a relatively normal posture, a high anomaly score is obtained due to unexpected appearance detection. Our method effectively detects this appearance anomaly.

**Motion Anomaly and Environment Disruption:** Figures 5 (2), (3) and (4) illustrate motion anomalies, specifically fighting, lying, and jaywalking. Particularly, the behavior of lying down is challenging for many algorithms to detect, but our algorithm can capture these motion anomalies. Additionally, our algorithm performs well in smoky or foggy conditions, which emphasizes the robustness of our approach in handling variations in environmental disruption.

### 4.5. Ablation Studies

**Ablation Study on Components and Loss Functions:** We analyze the contribution of each component and loss function and report the results in Table 2. From the first group of ablation experiments, we find that the LSTA module significantly improves model performance, while the BSMM module, is less impactful. This is attributed to the dataset's design, which is behavior and scene-independent in UBnormal datasets. Further experiments in Section 4.6 validate the effectiveness of the BSMM module. From the second group of experiments, we observe that both proposed loss functions are effective, with  $L_{mo}$  notably enhancing performance. This is primarily due to the fact that anomalies in human behavior are frequently associated with motion. The improvement in performance validates the effectiveness of our guidance-exploration pattern.

Table 2. Ablation experiments on modules and loss function.

Group	LSTA	BSMM	$L_{mo}$	$L_{app}$	SHT	UBN
			✓	✓	84.9	69.6
1	✓		✓	✓	86.5	73.5
		✓	✓	✓	85.1	69.4
2	✓	✓	✓		86.1	72.9
	✓	✓		✓	78.3	67.2
	✓	✓	✓	✓	<b>86.9</b>	<b>73.5</b>

Table 3. The AUC(%) performance of different types of measurement methods. ‘sim’ represents  $1 - (f_{rgb} \cdot f_{sk}) / (\|f_{rgb}\| \cdot \|f_{sk}\|)$ . Note that all methods require  $\|f\|$  in the end.

Method	$f_{sk}$	$f_{rgb}$	$f_{sk} + f_{rgb}$	sim	$f_{sk} - f_{rgb}$
SHT	83.8	81.2	67.7	<u>85.7</u>	<b>86.1</b>
UBN	64.5	66.5	50.7	<u>72.3</u>	<b>72.9</b>

**Feature Combination for Computing Anomaly Score:** As illustrated in Table 3, we conduct experiments to validate the effectiveness of our 1-st level guidance-exploration pattern and anomaly measurement methods. The results demonstrate that both similarity and Euclidean distance difference measurement methods have achieved good results, far surpassing other approaches. Furthermore, to depict the distribution of anomalies and normal samples, we plot histograms in Figure 6 for both the method utilizing feature  $f_{sk}$  generated by Normalizing Flow and our RGB Encoder. Our approach assigns higher scores to anomalies, highlighting the effectiveness of our guidance-exploration pattern. The comparison results for the 2-nd level are provided in the appendix.

#### 4.6. Explore the Capability of the Behavior-Scene Matching Memory

In existing datasets, anomalies related to scenes are relatively rare. Similar to [30], we adapt the dataset and perform the following experiments to assess the effectiveness of the Behavior-Scene Matching Method.

Initially, within the UBNormal dataset, the actions of “running” and “jumping” were deemed abnormal across all scenes. We consider these two actions as normal in the appropriate scenes. Firstly, we extract a subset from the UBNormal dataset, encompassing Scenes 1, 3, 4, 5, 11, 20 and 21. Subsequently, we categorize these scenes into four types: Outdoor street scenes A, Indoor station scenes B, Outdoor zebra crossing scenes C, and Indoor office scenes D. Following that, we posit that “running” and “jumping” are considered normal within scenes A and B. Subsequently, videos containing these behaviors and no other anomalies are moved from the test set to the training set. Finally, as shown in Table 4, we divide the mentioned data

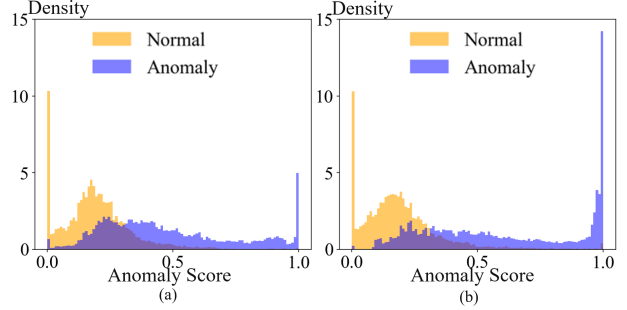


Figure 6. Histograms of anomaly scores for abnormal and normal data. (a) Normalizing Flow, (b) Our Guidance-Exploration Network in 1-st level.

Table 4. The AUC(%) performance of different methods. Here, A, B, C, and D are datasets derived from different scenes.

Method	[A,C,D]	[B,C,D]	[A,B,C,D]	Orign
Jigsaw [33]	58.2	59.7	61.0	57.1
STG-NF [16]	62.1	67.3	<u>65.8</u>	65.9
HF <sup>2</sup> -VAD [21]	59.2	58.0	59.9	62.4
<b>Our w/o BSMM</b>	<u>63.5</u>	<u>66.8</u>	65.1	<b>67.7</b>
<b>Our</b>	<b>64.1</b>	<b>68.2</b>	<b>67.1</b>	<u>67.2</u>

into three settings for both training and testing. Concurrently, we use the data from the original nine scenes as a control group.

As depicted in Table 4, our approach demonstrates superior performance improvement across the three experimental sets compared to the scenario where the Behavior-Scene Matching Memory is not employed. Furthermore, our method surpasses advanced methods with publicly accessible code, validating the effectiveness of our Behavior-Scene Matching Memory in identifying anomalies related to scenes.

## 5. Conclusion

We design a novel framework, the multilevel guidance-exploration framework, which combines RGB and skeletal features to detect various anomalies. First, guided by the Normalizing Flow, the RGB Encoder learns high-level motion features from unmasked frames. Simultaneously, guided by the RGB Encoder, the Mask Encoder distills appearance features using masked RGB frames. Then, motion and appearance anomalies are detected based on the similarity between high-level representations. Additionally, we also propose the Scene-Behavior Matching Module to explore the relationship between normal patterns of behaviors and scenes, enabling the detection of behavior anomalies related to scenes. Our approach achieves the best performance on the ShanghaiTech and UBnormal datasets.



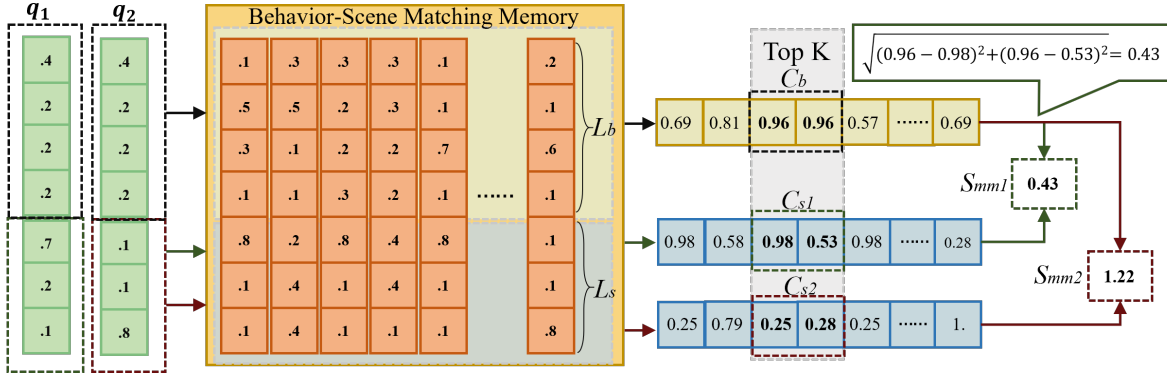


Figure 7. Flowchart of the BMSS read process and scene-related anomaly score calculation.

## 6. Further Elaboration on BSMM

As depicted in Figure 7 for clarity, we have created an explanatory diagram detailing the mechanism of the “read” process. Notably, in experiments, we calculate similarity weights between behavior and the first  $L_b$  channels of all memory items. We select the top  $K$  vectors with the highest similarity weights as matching weights  $C^b \in \mathbb{R}^K$  and compute scene-related anomaly scores with their corresponding scene similarity weights. In the experiments, we utilize the four datasets mentioned in Section 4.6 of the paper and split them into train, validation, and test sets with a 5:2:3 ratio. We perform hyperparameter tuning on the validation sets and select the optimal  $K$  values of 4. For this explanatory diagram, we assume a hypothetical value of  $K$  equal to 2.

Specifically, consider two query items with identical behavioral features but differing scene features, denoted as  $q_1$  and  $q_2$ . Initially, we compute the similarity between behavioral features and the first  $L_b$  channels of each item in the Behavior-scene Memory. Similarly, we calculate the similarity between scene features and the last  $L_s$  channels of each item in the Behavior-scene Memory. The results, as depicted in the figure 7 (without normalization for the illustrative figure), are then used to form matching weights  $C_b$  comprising the top  $K$  data points with the highest behavioral similarity. In the illustrative diagram, the behavioral features of the third and fourth items exhibit the highest similarity to those of the query. Next, we compute the distance between the behavior matching weights  $C^b$  and the corresponding scene similarity addressing weights  $C^s$  to derive the final scene-related anomaly score  $S_{mm}$ .

From the demonstration results, it is evident that for the query item  $q_2$ , the behavioral features are similar to the top  $K$  items in memory. However, the scene features exhibit low similarity with the last  $L_s$  channels of memory items, indicating a scene-related anomaly.

## References

- [1] Andra Acsintoae, Andrei Florescu, Mariana-Iuliana Georgescu, Tudor Mare, Paul Sumedrea, Radu Tudor Ionescu, Fahad Shahbaz Khan, and Mubarak Shah. Ub-normal: New benchmark for supervised open-set video anomaly detection. In *CVPR*, pages 20143–20153, 2022. 6
- [2] Anurag Arnab, Mostafa Dehghani, Georg Heigold, Chen Sun, Mario Lučić, and Cordelia Schmid. Vivit: A video vision transformer. In *Proceedings of the IEEE/CVF international conference on computer vision*, pages 6836–6846, 2021. 4
- [3] Hangbo Bao, Li Dong, Songhao Piao, and Furu Wei. Beit: Bert pre-training of image transformers. *arXiv preprint arXiv:2106.08254*, 2021. 3, 4
- [4] Antonio Barbalau, Radu Tudor Ionescu, Mariana-Iuliana Georgescu, Jacob Dueholm, Bharathkumar Ramachandra, Kamal Nasrollahi, Fahad Shahbaz Khan, Thomas B Moeslund, and Mubarak Shah. Ssm++: Revisiting self-supervised multi-task learning for video anomaly detection. *Computer Vision and Image Understanding*, 229:103656, 2023. 1, 2, 7
- [5] Bertasius. Is space-time attention all you need for video understanding? In *ICML*, page 4, 2021. 7
- [6] Ruichu Cai, Hao Zhang, Wen Liu, Shenghua Gao, and Zhifeng Hao. Appearance-motion memory consistency network for video anomaly detection. In *Proceedings of the AAAI conference on artificial intelligence*, pages 938–946, 2021. 1, 2, 7
- [7] Yunpeng Chang, Zhigang Tu, Wei Xie, Bin Luo, Shifu Zhang, Haigang Sui, and Junsong Yuan. Video anomaly detection with spatio-temporal dissociation. *Pattern Recognition*, 122:108213, 2022. 4
- [8] Chengwei Chen, Yuan Xie, Shaohui Lin, Angela Yao, Guan-nan Jiang, Wei Zhang, Yanyun Qu, Ruizhi Qiao, Bo Ren, and Lizhuang Ma. Comprehensive regularization in a bi-directional predictive network for video anomaly detection. In *Proceedings of the AAAI Conference on Artificial Intelligence*, pages 230–238, 2022. 2
- [9] Xiaokang Chen, Mingyu Ding, Xiaodi Wang, Ying Xin, Shentong Mo, Yunhao Wang, Shumin Han, Ping Luo, Gang

- Zeng, and Jingdong Wang. Context autoencoder for self-supervised representation learning. *International Journal of Computer Vision*, pages 1–16, 2023. 3
- [10] Alexey Dosovitskiy, Lucas Beyer, Alexander Kolesnikov, Dirk Weissenborn, Xiaohua Zhai, Thomas Unterthiner, Mostafa Dehghani, Matthias Minderer, Georg Heigold, Sylvain Gelly, et al. An image is worth 16x16 words: Transformers for image recognition at scale. *arXiv preprint arXiv:2010.11929*, 2020. 4
- [11] Hao-Shu Fang, Jiefeng Li, Hongyang Tang, Chao Xu, Haoyi Zhu, Yuliang Xiu, Yong-Lu Li, and Cewu Lu. Alpha-pose: Whole-body regional multi-person pose estimation and tracking in real-time. *IEEE Transactions on Pattern Analysis and Machine Intelligence*, 2022. 3
- [12] Feng. Mist: Multiple instance self-training framework for video anomaly detection. In *CVPR*, pages 14009–14018, 2021. 7
- [13] Alessandro Flaborea, Guido Maria D’Amely di Melenugno, Stefano D’arrigo, Marco Aurelio Sterpa, Alessio Sampieri, and Fabio Galasso. Contracting skeletal kinematic embeddings for anomaly detection. *arXiv preprint arXiv:2301.09489*, 2023. 7
- [14] Mariana-Iuliana Georgescu, Antonio Barbalau, Radu Tudor Ionescu, Fahad Shahbaz Khan, Marius Popescu, and Mubarak Shah. Anomaly detection in video via self-supervised and multi-task learning. In *CVPR*, pages 12742–12752, 2021. 1, 2
- [15] Mariana Iuliana Georgescu, Radu Tudor Ionescu, Fahad Shahbaz Khan, Marius Popescu, and Mubarak Shah. A background-agnostic framework with adversarial training for abnormal event detection in video. *IEEE transactions on pattern analysis and machine intelligence*, 44(9):4505–4523, 2022. 7
- [16] Hirschorn. Normalizing flows for human pose anomaly detection. *arXiv preprint arXiv:2211.10946*, 2022. 1, 2, 4, 6, 7, 8
- [17] Xiangyu Huang, Caidan Zhao, and Zhiqiang Wu. A video anomaly detection framework based on appearance-motion semantics representation consistency. In *ICASSP 2023-2023 IEEE International Conference on Acoustics, Speech and Signal Processing (ICASSP)*, pages 1–5. IEEE, 2023. 1, 2, 7
- [18] Jungho Lee, Minhyeok Lee, Dogyoon Lee, and Sangyoun Lee. Hierarchically decomposed graph convolutional networks for skeleton-based action recognition. In *Proceedings of the IEEE/CVF International Conference on Computer Vision*, pages 10444–10453, 2023. 4
- [19] Shuo Li, Fang Liu, and Licheng Jiao. Self-training multi-sequence learning with transformer for weakly supervised video anomaly detection. In *AAAI*, pages 1395–1403, 2022. 7
- [20] Wen Liu, Weixin Luo, Dongze Lian, and Shenghua Gao. Future frame prediction for anomaly detection—a new baseline. In *CVPR*, pages 6536–6545, 2018. 1, 2
- [21] Zhian Liu, Yongwei Nie, Chengjiang Long, Qing Zhang, and Guiqing Li. A hybrid video anomaly detection framework via memory-augmented flow reconstruction and flow-guided frame prediction. In *CVPR*, pages 13588–13597, 2021. 1, 2, 7, 8
- [22] Weixin Luo, Wen Liu, and Shenghua Gao. A revisit of sparse coding based anomaly detection in stacked rnn framework. In *Proceedings of the IEEE international conference on computer vision*, pages 341–349, 2017. 6
- [23] Amir Markovitz, Gilad Sharir, Itamar Friedman, Lih Zelnik-Manor, and Shai Avidan. Graph embedded pose clustering for anomaly detection. In *CVPR*, pages 10539–10547, 2020. 7
- [24] Romero Morais, Vuong Le, Truyen Tran, Budhaditya Saha, Moussa Mansour, and Svetha Venkatesh. Learning regularity in skeleton trajectories for anomaly detection in videos. In *CVPR*, pages 11996–12004, 2019. 7
- [25] Hyunjong Park, Jongyoun Noh, and Bumsub Ham. Learning memory-guided normality for anomaly detection. In *CVPR*, pages 14372–14381, 2020. 1, 2, 5
- [26] Nicolae-Cătălin Ristea, Neelu Madan, Radu Tudor Ionescu, Kamal Nasrollahi, Fahad Shahbaz Khan, Thomas B Moeslund, and Mubarak Shah. sspcab. In *CVPR*, pages 13576–13586, 2022. 1, 2, 7
- [27] Marco Rudolph, Tom Wehrbein, Bodo Rosenhahn, and Bastian Wandt. Asymmetric student-teacher networks for industrial anomaly detection. In *Proceedings of the IEEE/CVF Winter Conference on Applications of Computer Vision*, pages 2592–2602, 2023. 2
- [28] Sultani. Real-world anomaly detection in surveillance videos. In *CVPR*, pages 6479–6488, 2018. 7
- [29] Shengyang Sun and Xiaojin Gong. Long-short temporal co-teaching for weakly supervised video anomaly detection. *arXiv preprint arXiv:2303.18044*, 2023. 6, 7
- [30] Shengyang Sun and Xiaojin Gong. Hierarchical semantic contrast for scene-aware video anomaly detection. In *CVPR*, pages 22846–22856, 2023. 1, 2, 5, 7, 8
- [31] Yu Tian, Guansong Pang, Yuanhong Chen, Rajvinder Singh, Johan W Verjans, and Gustavo Carneiro. Weakly-supervised video anomaly detection with robust temporal feature magnitude learning. In *ICCV*, pages 4975–4986, 2021. 7
- [32] Zhan Tong, Yibing Song, Jue Wang, and Limin Wang. Videomae: Masked autoencoders are data-efficient learners for self-supervised video pre-training. *Advances in neural information processing systems*, 35:10078–10093, 2022. 3, 4
- [33] Guodong Wang and Wang. Video anomaly detection by solving decoupled spatio-temporal jigsaw puzzles. In *ECCV*, pages 494–511. Springer, 2022. 1, 2, 7, 8
- [34] Rui Wang, Dongdong Chen, Zuxuan Wu, Yinpeng Chen, Xiyang Dai, Mengchen Liu, Lu Yuan, and Yu-Gang Jiang. Masked video distillation: Rethinking masked feature modeling for self-supervised video representation learning. In *Proceedings of the IEEE/CVF Conference on Computer Vision and Pattern Recognition*, pages 6312–6322, 2023. 3
- [35] Yizhou Wang, Can Qin, Yue Bai, Yi Xu, Xu Ma, and Yun Fu. Making reconstruction-based method great again for video anomaly detection. In *2022 IEEE International Conference on Data Mining (ICDM)*, pages 1215–1220. IEEE, 2022. 1, 7
- [36] Longhui Wei, Lingxi Xie, Wengang Zhou, Houqiang Li, and Qi Tian. Mvp: Multimodality-guided visual pre-training. In

- European Conference on Computer Vision*, pages 337–353. Springer, 2022. 3
- [37] Peng Wu and Jing Liu. Learning causal temporal relation and feature discrimination for anomaly detection. *IEEE Transactions on Image Processing*, 30:3513–3527, 2021. 1
- [38] Zhenda Xie, Zheng Zhang, Yue Cao, Yutong Lin, Jianmin Bao, Zhuliang Yao, Qi Dai, and Han Hu. Simmim: A simple framework for masked image modeling. In *Proceedings of the IEEE/CVF Conference on Computer Vision and Pattern Recognition*, pages 9653–9663, 2022. 4
- [39] Yuliang Xiu, Jiefeng Li, Haoyu Wang, Yinghong Fang, and Cewu Lu. Pose Flow: Efficient online pose tracking. In *BMVC*, 2018. 3
- [40] Shinji Yamada, Satoshi Kamiya, and Kazuhiro Hotta. Reconstructed student-teacher and discriminative networks for anomaly detection. In *2022 IEEE/RSJ International Conference on Intelligent Robots and Systems (IROS)*, pages 2725–2732. IEEE, 2022. 2
- [41] Sijie Yan, Yuanjun Xiong, and Dahua Lin. Spatial temporal graph convolutional networks for skeleton-based action recognition. In *Proceedings of the AAAI conference on artificial intelligence*, 2018. 4
- [42] Zhiwei Yang, Jing Liu, Zhaoyang Wu, Peng Wu, and Xiaotao Liu. Video event restoration based on keyframes for video anomaly detection. In *CVPR*, pages 14592–14601, 2023. 1, 2, 7
- [43] M Zaigham Zaheer, Arif Mahmood, M Haris Khan, Matia Segu, Fisher Yu, and Seung-Ik Lee. Generative cooperative learning for unsupervised video anomaly detection. In *CVPR*, pages 14744–14754, 2022. 1
- [44] Xinyu Zhang, Jiahui Chen, Junkun Yuan, Qiang Chen, Jian Wang, Xiaodi Wang, Shumin Han, Xiaokang Chen, Jimin Pi, Kun Yao, et al. Cae v2: Context autoencoder with clip target. *arXiv preprint arXiv:2211.09799*, 2022. 3